SCIENTIFIC REPORTS

OPEN

SUBJECT AREAS:
COMPOSITES
SYNTHESIS AND PROCESSING

Received
23 December 2013

Accepted
4 March 2014

Published
20 March 2014

Correspondence and requests for materials should be addressed to W.L.L. (wenle@vt.edu) or J.Y.W. (john.walz@uky.edu)

Porous Nanocomposites with Integrated Internal Domains: Application to Separation Membranes

Wenle Li[1] & John Y. Walz[2]

[1]127 Randolph Hall, Department of Chemical Engineering, Virginia Tech, Blacksburg, VA 24061, USA, [2]353 RGAN, College of Engineering, University of Kentucky, Lexington, KY 40506, USA.

Asymmetric membranes with layered structure have made significant achievements due to their balanced properties and multi-functionalities that come from a combination of multiple layers. However, issues such as delamination and substructure resistance are generated by the intrinsic layered structure. Here, we present a strategy to integrate the traditional layered structure into an asymmetric but continuous porous network. Through infiltrations of microparticles and nanoparticles to targeted regions, active domains are created inside the porous scaffold versus having them applied externally. The fabricated internal active domains are highly adjustable in terms of its dimensions, pore size, and materials. We demonstrate that it is a general method that can be applicable to a wide variety of particles regardless of their material, dimensions, or geometry. By eliminating the external layered structure, problems such as those mentioned above can be eliminated. This integration technique can be extended to other devices required a layered structure, such as solid oxide fuel cells and lithium ion battery.

A great deal of effort has been devoted over the past decades toward the development and manufacture of membranes, driven primarily by their applicability and relatively low energy requirements compared to other techniques[1–3]. Membranes can be constructed from a wide variety of materials, including organics[1,4,5], inorganics[6–8], and organic-inorganic composites[9], and are typically classified as either dense or porous, depending on their structure. Although the dense (non-porous) membranes are known for their high selectivity for gas separation, their industrial applications are limited by low permeability[8]. In comparison, porous membranes are more widely applicable because the balance between permeability and selectivity can be controlled by adjusting the pore size.

Asymmetric porosity is one of the most common structures for porous membranes[8]. Typical asymmetric membranes consist of a layered structure in which one side of the membrane contains a thin active layer where most separation occurs, while the majority of the membrane provides support and mechanical strength[7,10,11]. Pores in the support layer are typically orders of magnitude larger than those in the active layer in order to avoid compromising the overall permeability. Intermediate layers with gradients in pore size are frequently used to connect the support and active layers[10]. Due to this combination of multiple layers with different functionalities, asymmetric porous membranes possess balanced permeability, selectivity, and mechanical integrity.

In addition to the size-dependent selectivity, chemical selectivity based on charge[11], hydrophobicity[12], chirality[13], or pH-sensitivity[14], all of which can be achieved by functionalizing the active layer[15], provides porous membranes additional avenues for improved efficiency and expanded applications. To date, application of asymmetric membranes has made progress in such fields as water purification, drug delivery, biomolecule separation, electronic industries, dairy, and food[15–18].

In spite of the achievements reached in asymmetric porous membranes, several issues remain because of the intrinsic layered structure. First, a higher chance of delamination exists at the interfaces under external pressure, and additional efforts are needed to improve the adhesion[19–21]. Second, substructure resistance generated by the mismatch of porosities between layers can reduce the permeability of the membrane[19,20]. Third, the mismatch of the thermal expansion coefficients between layers undermines the durability of the membranes under applied thermal, tensile, or compressive loads[10]. Fourth, material candidates for each layer are greatly limited in consideration of their similarity in characteristics. As a result of these issues, it is challenging to develop membranes with synergistic combinations of functions that incorporate different kinds of materials into the active layer. Moreover, cost-effective methods for producing high efficiency membranes require further investigation[22].

In this work, we present a versatile strategy for developing asymmetric membranes with a highly adjustable active domain. Instead of constructing membranes layer by layer, we infiltrate microparticles and nanoparticles into a given porous scaffold such that the active domain is actually formed inside the porous support structure versus having it applied externally. This approach avoids problems with adhesion of the active layers, reduces the probability of delamination, and eliminates the substructure resistance at the interfaces. We demonstrate that this method works very well for a variety of particles, regardless of the size, shape, or materials. This general applicability makes this strategy effective in fabricating membranes with controllable properties (e.g. pore size, surface area, surface properties, permeability). Through infiltration of particles of varying materials, membranes with multiple functions can be fabricated. Furthermore, the synthesis method consists of a series of straightforward techniques, making it promising for large-scale applications.

Results

Fabrication of the internal domains. Our fabrication method for asymmetric membrane with internal active domains is a three-step process (Figure 1). First, a porous scaffold with ~35 mm diameter and ~450 μm thickness is prepared by freeze drying and sintering of an aqueous suspension containing kaolinite and silica. Second, an internal active domain is created by infiltrating a microparticle solution into the porous scaffold and then drying from one side of the membrane such that evaporation pulls the particles to the open side. Finally, a nanoparticle solution is spin-coated onto the microparticle surface such that the nanoparticles are deposited into the interstitial spaces between the microparticles, forming an internal, nano-scale active domain that is free from defects.

The membrane scaffolds were fabricated by applying freeze-drying to suspensions containing 10 vol% kaolinite and 8 vol% silica (i.e., this particular composition was found in prior work to provide improved microstructure and the best flexural strength)[23–25]. During freezing, the mold serves as a cold finger (the thermal conductivity of stainless steel mold is much larger than that of air), such that directional freezing is generated. As a result, a hierarchical porous microstructure is created[26,27]. At the beginning of solidification, ice crystals nucleate at the cold finger and small pores with an average size of ~2 μm are created after removal of ice crystals (Figure 2a). In the region away from the cold finger, pores become larger as the ice crystals grow with the continuous freezing (Figure 2b). It should be noted that the pores throughout the scaffold are either spherical or elongated (Figure 2a, b). Because of the relatively low temperature gradient, pores are created instead of channels (i.e., the disk-like kaolinite particles are not completely expelled from the freezing front[25]). The membranes were finally sintered at 1250°C for 1 h to improve the mechanical strength, yielding a structure with a porosity of ~70%[24,32].The pores of the structure are interconnected as tests have shown that water can easily pass through the structure under a small pressure.

The stainless steel mold used in this work was equipped with an adjustable depth (Supporting Information, Figure S1), which allowed creating scaffolds with thickness ranges from 200 μm to 500 μm (comparable to that of typical freeze-tape-casting). Figure 2b shows the cross-section microstructure of a typical scaffold. The top region with small pores (i.e., ~2 μm) occupies roughly ¼ of the overall thickness. It should be mentioned that the active layers described below were created in the region of the scaffold where the pores were the smallest.

In this work, two methods were used to infiltrate microparticles into the porous scaffold: (1) immersion the entire porous scaffold into an aqueous suspension containing a controlled concentration of microparticles, (2) placing drops of the suspension onto the porous scaffold from the open side. Both methods were found to be effective, although the second was primarily applied to create the samples used in this work because it required a smaller amount of suspension and microparticles. The membrane scaffold was placed on a flat dish with the side with the small pores exposed to air. During drying, evaporation occurs primarily from the open surface (i.e., top surface), as the bottom is covered and the sides are orders of magnitude thinner. As evaporation proceeds, water moves upward toward the open surface, transporting the suspended particles that pack into a thin layer (Figure 2c). The membrane was therefore treated at 1000°C for 2 h to secure the microparticles in place. The active domain created in this work is different from the traditional layer-by-layer membranes as it builds an internal region at one side of the scaffold (Figure 2d). By observing the cross-section of the membranes, the particles are found to fill the top pores of the scaffold with a typical layer thickness that is less than 3 μm. Peeling off a few microns of the top surface and imaging the layers beneath revealed few infiltrating microparticles, confirming that the particles are indeed concentrated at the top face of the membrane (Supporting Information, Figure S2). The porosity within this internal layer of microparticles was estimated by nitrogen adsorption measurements of pore volume, coupled with the known average membrane density, to be 19.3%. This value is consistent with

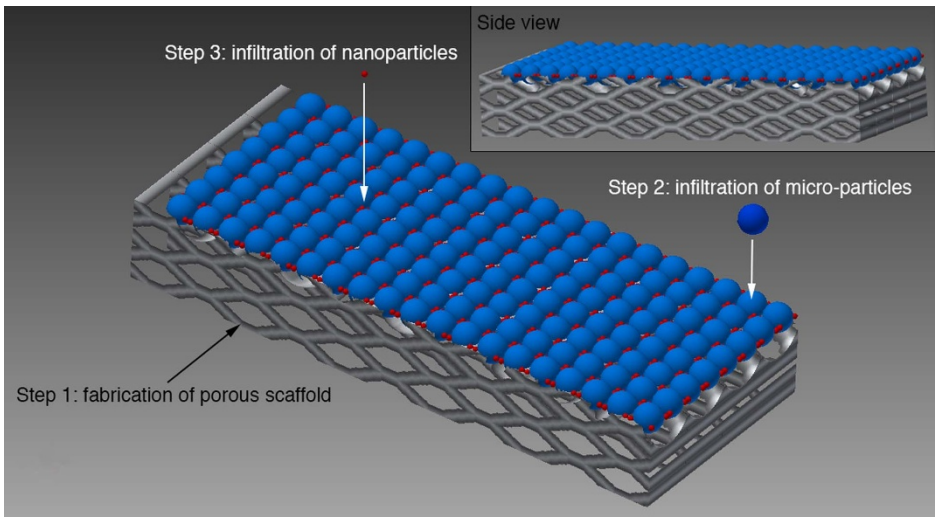

Figure 1 | Step-by-step illustration of the procedure used to develop the internal domains in the membrane. (1) Preparation of porous scaffold, (2) infiltration of micro-particles, (3) infiltration of nanoparticles. The insert displays the side view of the final structure.

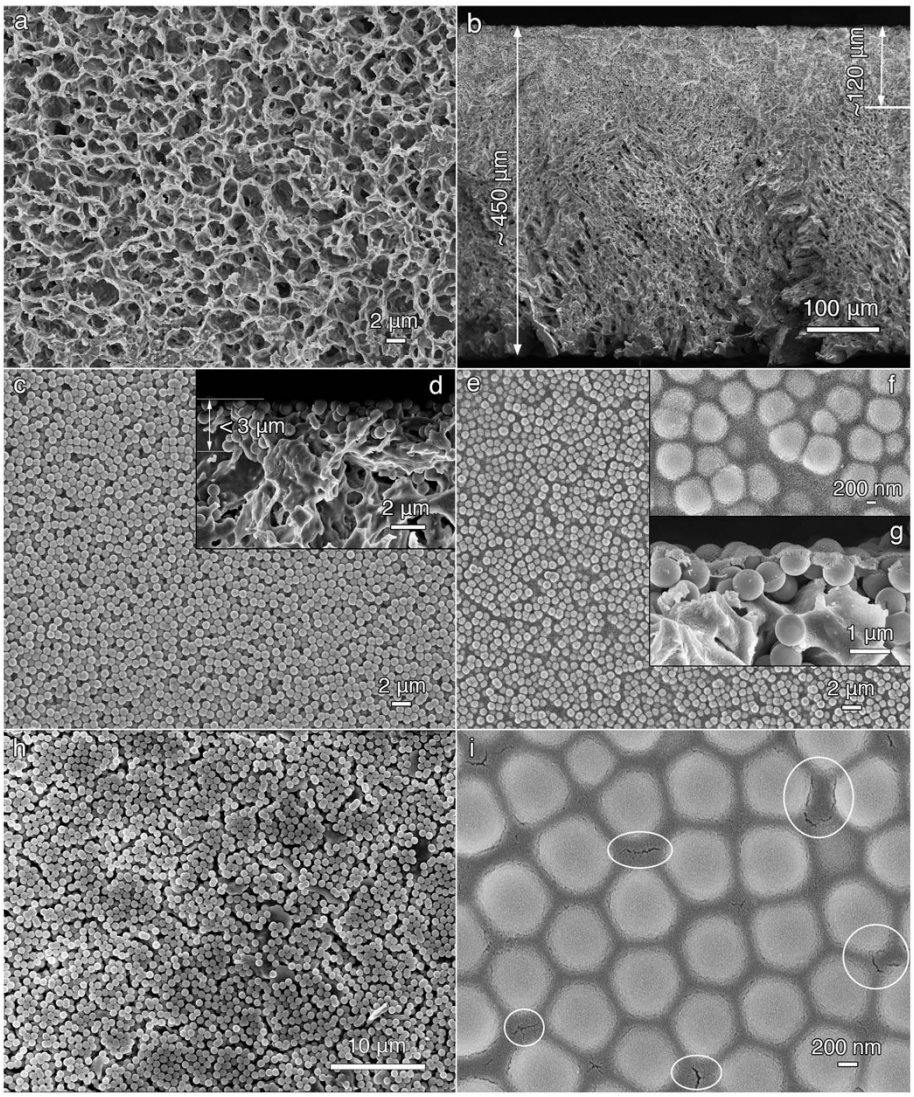

Figure 2 | Step-course monitoring of the fabrication of internal active domains by SEM. Microstructures of: (a) surface of the as-prepared scaffold with the smaller pores, (b) cross-section of the as-prepared porous scaffold showing the variation in pore size, (c) surface and (d) cross-section of the membrane with 1 μm silica particle infiltrated, (e), (f) surface and (g) cross-section of the membrane with 6 nm silica particle infiltrated internal domain, (h) surface of 1 μm silica particle domain formed without PVP addition showing cracks in the particle film, (i) surface of 6 nm silica particle domain formed without PVP addition showing cracks in the particle film.

values calculated assuming close packing of the spheres in this internal layer.

The reason for the need to form this microporous domain is that it was found that the size of the infiltrating particles must be roughly the same order of magnitude as that of the pores, otherwise a uniform and durable layer of particles cannot be achieved. Thus in order to successfully create an active domain with nanoparticles (e.g., 6 nm diameter), it was first necessary to create pores smaller than the 2 μm characteristic size of the scaffold support.

The procedure that was used to create the nanoparticle domain in the interstitial space between the infiltrated microparticles proved effective in not only producing a homogeneous nanoparticle layer but also precisely controlling its thickness. This was accomplished by allowing the nanoparticle suspension to access only a very thin region near the upper area of the microparticle region. Specifically, after a several micron-thick layer of microparticles had been created near one face of the membranes, the entire structure was rendered hydrophobic by exposure to a trimethylchlorosilane (TMCS) vapor (elaborated in Methods). Afterwards, a very thin layer of the hydrophobic membrane was made hydrophilic by immersion into a piranha solution for a brief period of time. It was found that this step created a hydrophilic layer whose thickness could be adjusted by controlling both the concentration of the piranha solution and the soaking time in the solution. The nanoparticle suspension was subsequently spin-coated onto the microparticle region (i.e., top) of the membrane. During this step, the suspension only penetrated into the thin hydrophilic layer. Finally, the membrane was allowed to air dry and then subjected to a mild sintering (850°C for 4 h) to fuse the nanoparticles into place.

It was found that this procedure yielded a very thin layer of nanoparticles near the upper surface of the membrane (Figure 2g). As can be seen, the very top microparticles are bridged by the closely packed nanoparticles (Figure 2e, f). BET measurements on these samples revealed peaks at pore sizes of ~3.5, ~4.5, ~7.0 and ~13.0 nm (Supporting Information, Figure S3). The porosity of this nanoparticle layer was estimated using nitrogen adsorption measurement as 5.1%, which again is consistent with values predicted assuming close packing of the nanoparticles in the layer. From the cross-sectional view (Figure 2g), the nanoparticle domain was found to be of quite uniform throughout the top surface, with a thickness of ~200 nm.

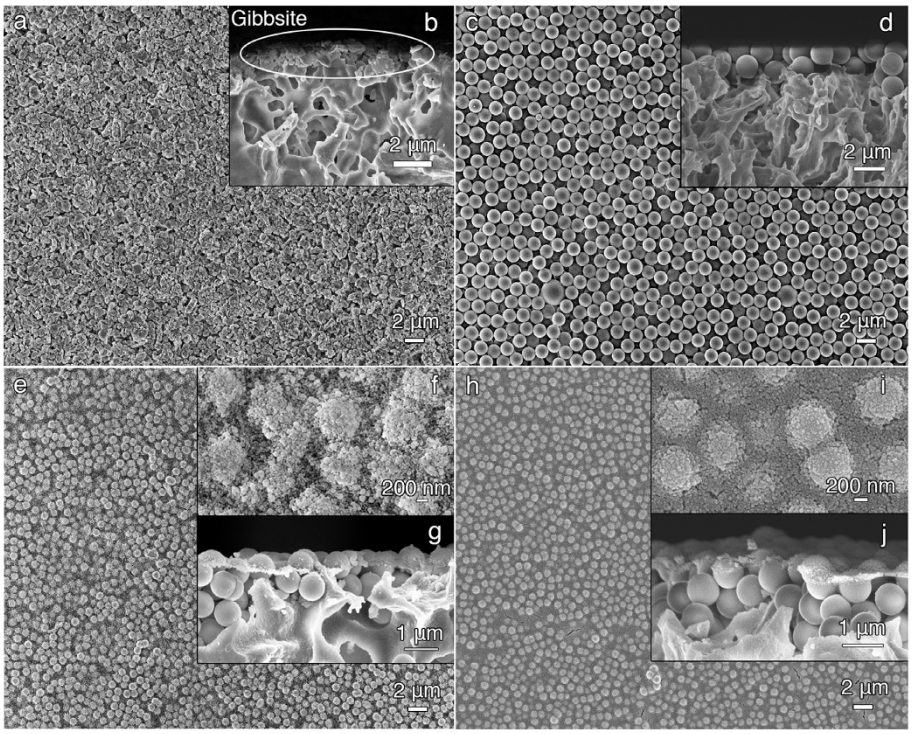

Figure 3 | Internal active domains created by a variety of particles. Microstructures of: (a) surface and (b) cross-section of the membrane with 0.56 μm gibbsite particles infiltrated, (c) surface and (d) cross-section of the membrane with 1.6 μm latex particles infiltrated, (e), (f) surface and (g) cross-section of the membrane with 85 nm silica particles infiltrated, (h), (i) surface and (j) cross-section of the membrane with 20 nm latex particles infiltrated.

Again, as mentioned previously, the thickness of this domain could be adjusted by controlling the thickness of the hydrophilic region and the parameters of spin coating.

One issue associated with this infiltration/spin coating and air-drying method is cracks that form on the top surface. This is a common problem in particle films and arises from the strong capillary pressures created during air drying[28]. As shown in Figure 2h, i, both microparticles and nanoparticles would crack if they were dried directly after either infiltration or spin coating. Since hard particles will inevitably fracture during drying, crack-free particle films can be obtained by 'softening' the particles[28]. In this work, we introduced the polymer polyvinylpyrrolidone (PVP) when preparing both the microparticle and nanoparticle suspensions. The PVP layer provides a cushion that can deform to relieve the stress and inhibit cracks[28,29]. As a result, both microparticle and nanoparticle domains created by suspension with PVP addition show crack-free homogeneous packing (Figure 2e–g). The PVP molecules burn off during the subsequent sintering step.

General applicability. One advantage of this strategy lies in its general applicability to different kinds of particles, regardless of the size, geometry, or material. Two kinds of microparticles, irregular-shaped gibbsite particles with an average size of 0.56 μm and sulfate latex spherical particles with 1.6 μm diameter, were firstly infiltrated directly to the porous scaffold to demonstrate this general capability in creating microparticle internal domain. As shown in Figure 3a–d, both top surfaces of the resulting membranes are uniform with packed particles, and the internal active domains are each of a thickness less 3 μm. It should be mentioned that some of the sulfate latex particles are actually on top of the scaffold because its size (1.6 μm) is comparable to that of the pores (~2 μm). This suggests that there is an upper limit of particle sizes that can be used to create an internal domain. As discussed above, it was also found in subsequent tests that the internal particle film could not be formed when the particles were too small. For the particular scaffolds used here (~2 μm pore size), this lower limit was found to be a particle diameter of approximately 0.5 μm. In addition to the adjustable particle size, the success with the gibbsite demonstrates that the method can be applied to irregularly-shaped particles as well. Moreover, the sulfate latex particles demonstrate that organic particles can be used.

As for the creation of nanoparticle internal domain, 85 nm silica particles and 20 nm amidine latex particles were used to demonstrate the general applicability to different kinds of nanoparticles. These two nanoparticles were utilized to create the nanoparticle domain in the interstitial space between the infiltrated microparticles, following the methods discussed above. In both cases, crack free homogeneous film of nanoparticles were fabricated with thicknesses of ~200 nm (Figure 3e–j).

It should be motioned that both 1.6 μm and 20 nm latex particle domains were created without PVP addition in the suspensions. This is because latex particles cannot withstand the sintering temperatures used with the silica nanoparticles. As a result, a few small cracks appear in the 20 nm latex particle film (Figure 3h, i).

The success in applying this technique to different types of particles suggests its contribution to fields other than separation membranes. For instance, solid oxide fuel cell (SOFC) cathodes with infiltrated active components were shown to have improved performances[30]. With our method, infiltration of these active components can be more precisely controlled. In addition, the traditional layered structure SOFC can be integrated into a one-piece device by infiltrating cathode and anode materials into two sides of a porous electrolyte. This configuration is promising in removal of the problems associated with the interfaces, and the three-dimensional network structure could promote the transport of the electron carriers. Also, the same design can be applicable to lithium ion batteries with solid electrolyte.

Membrane performances. To characterize the performances of our membrane, water flux and filtration tests were also performed. Either deionized water or a 0.01 vol% silica nanoparticle aqueous suspension was applied to the membrane under fixed differential pressures (0.3 bar to 0.5 bar). The water that passed through a certain area of the membrane in a specific time period was collected and weighed, allowing calculation of the membrane's permeability (volume/area-time-pressure). As shown in Figure 4a, the membrane scaffold has a very high permeability of 203800 ± 5400 L/(m^2-h-bar). When an internal domain of 1 μm particles was created in the structure, the permeability dropped to 20200 ± 1400 L/(m^2-h-bar). When an additional domain of 6 nm nanoparticles was created, the permeability reduced further to 3300 ± 400 L/(m^2-h-bar).

Nonetheless, even this lower permeability value is still comparable to or higher than values reported by other researchers for membranes with nanometer-scale pores. For example, Hendren *et al.* reported a permeability of 400 L/(m^2-h-bar) for membranes with average pore size of 20 nm[31]. Ke *et al.* fabricated membranes having a permeability of 3000 to 4500 L/(m^2-h-bar) with a pore size of ~60 nm using nanofibers[16]. Even with much a smaller pore size in the active layer, we were able to achieve permeabilities comparable to these values.

Figure 4b–d show microstructures of the membrane surface (internal active domain side) after filtration of 0.01 vol% nanoparticle aqueous suspensions containing nanoparticles with sizes of 100 nm, 22 nm, or 12 nm, respectively. It is demonstrated that a membrane with 6 nm particle internal domain is effective in blocking the penetration of all three different sized particles.

The rejection rate of 22 nm and 12 nm nanoparticles was calculated by measuring the concentration of nanoparticles in the feed and filtrate solutions using the intensity of light scattered by the solutions. For the 100 nm nanoparticles, the concentration in the filtrate was too low to be measured using this technique. Instead, the rejection rate was calculated by measuring, using SEM, the number of particles per unit area that were deposited when a diluted drop of the suspension was placed on a slide and dried.

The membrane could filter 99.90% of the 100 nm silica particles, 99.52% of the 22 nm silica particles, and 76.26% of the 12 nm silica particle under differential pressure of 0.5 bar (Figure 5). The near complete rejection of particles with size above 22 nm validates the uniformity of the nanoscale internal active layer. Further validation was obtained by imaging the membrane surface under SEM at randomly chosen spots. Since the pore size of the internal active domain is determined by the size of the infiltrated nanoparticles, the cut-off size of the membrane is therefore adjustable. The small cut-off size and high permeability demonstrates the efficiency of these membranes.

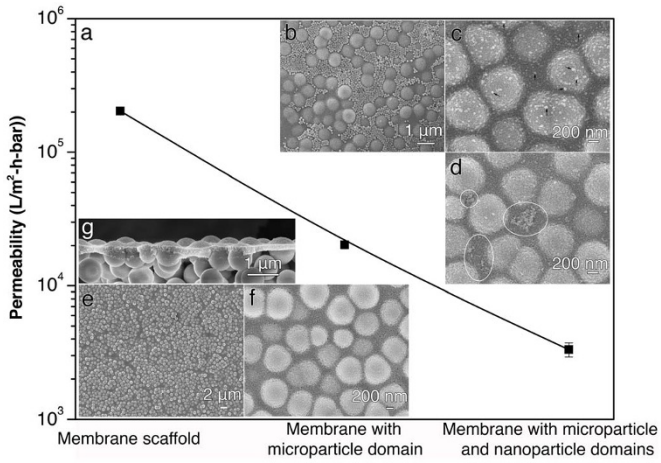

Figure 4 | Performances of the nanocomposites as a separation membrane. This graph (a) shows how the permeability of the membranes changes upon infiltrating particles to create the internal domains. The error bars correspond to the standard deviations of five measurements for each data point. The insets are scanning electron micrographs showing surface microstructure of the membrane created with 6 nm particle internal domain after a filtration test using (b) 100 nm particle suspension, (c) 22 nm particle suspension, and (d) 12 nm particle suspension. The remaining images show the surface (e), (f) and cross-section (g) of the membrane after exposure of the membrane to a differential pressure of 1 bar for 30 min.

The ability to remove the captured particles from the membrane using backwashing was also investigated, as this is a commonly-used industrial practice. SEM images of the surface after backwashing with deionized water showed no traces of either 12 nm, 22 nm or 100 nm nanoparticles, indicating the effectiveness of this cleaning technique. (Supporting Information, Figure S5).

Finally, in order to probe the integrity of the membrane, tests were performed in which differential pressures up to 1 bar were applied to the membrane for an accumulated period of 30 min. The microstructure of both the top surface (Figure 4e, f) and the cross-section (Figure 4g) were then examined. As seen, by comparing these images to those show in Figure 3e–g, taken on samples that had not been tested, no discernible changes could be detected, providing evidence of the integrity and durability of the membranes.

Discussion

We have developed a strategy involving straightforward synthesis techniques for creating membranes with a unique internal active domain structure. The active domain is actually contained within the supporting scaffold rather than as an external layer, as is typical for asymmetric membranes. This structure is created by infiltrating a microparticle solution into the porous scaffold and then drying from one side of the membrane such that evaporation pulls the microparticles to the open side. Afterward, a nanoparticle domain is subsequently spin-coated into the microparticle film. By controlling the spatial variation in hydrophobicity of the structure, the nanoparticles are confined to the upper region of the microparticle layer. The resulting active domains are of a thickness less than 1% of that of the membrane for microparticles and even smaller for nanoparticles. The elimination of the layered structure effectively reduces the substructure resistance and the probability of delamination under differential pressure or thermal treatment. As a result, a membrane with high permeability and excellent durability is produced.

Crack-free particle domains were achieved by adding PVP into the infiltrating particle suspensions to soften the particle interactions during drying. We have also demonstrated that this strategy works effectively with a large variety of particles, regardless of their size (micron to nanometer), shape (spherical and irregular shaped), or material (inorganic and organic). The general applicability suggests that this strategy is promising in constructing the next generation of membranes with both high efficiency and synergistic combinations of functions. By infiltrating a mixture of different particles to build the active domain, membranes with multiple chemical selectivities and other functions (e.g. photocatalytic decomposition, magnetic adsorption) could be created. Furthermore, the idea of an integrated structure is also promising for other multi-layered devices, such as SOFC and lithium ion batteries.

Methods

Materials. The porous scaffolds for the membranes were created using a 34 wt% silica nanoparticle suspension (Ludox TMA, Sigma Aldrich, St. Louis, MO), kaolinite powder (Hydrite Flat-D, Imerys Performance Materials, Dry Branch, GA), sodium chloride (NaCl, AR grade, Mallinckrodt, Paris, KY), sodium hydroxide (NaOH, Mallinckrodt, Paris, KY), and de-ionized water, each of which was used without further purification. The silica nanoparticles had an average diameter of 22 nm and a density of 2.37 g/cm^3, while the kaolinite particles were disk-like with observed diameters ranging from 200 nm to 6 μm and a measured density of 2.56 g/cm^3.

Silica microspheres with average sizes of 1 μm (Polyscience Inc., Warrington, PA), gibbsite powders (hydrated alumina, aluminum tri-hydroxide, Almatis Inc.,

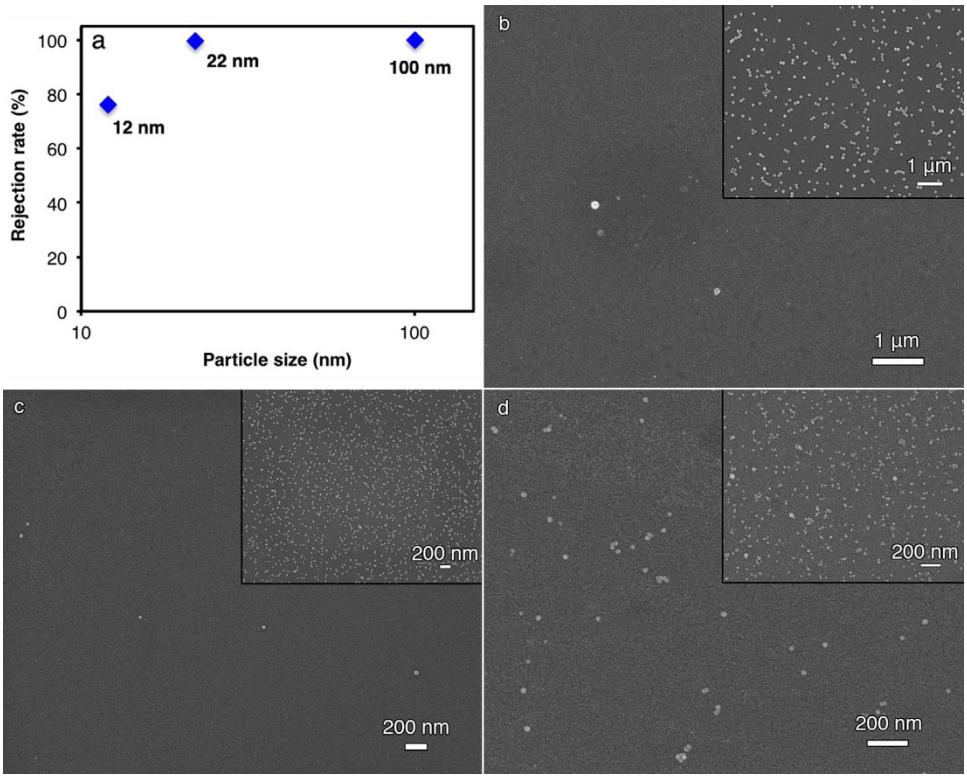

Figure 5 | Rejection rates of three different nanoparticle sizes obtained using a membrane that had been infiltrated with 1 μm and 6 nm particles. (a) Rejection rates as a function of particle size. SEM images obtained from samples of suspensions of (b) 100 nm, (c) 22 nm, and (d) 12 nm nanoparticles that had been diluted and dried. In each image, the insert was obtained using a sample of the feed solution while the larger image was obtained using the filtrate.

Frankfurt, Germany), and sulfate latex microspheres with average size of 1.6 μm (Invitrogen, Life Technologies, Grand Island, NY) were used as infiltrating particles to fabricate the micro-scale internal layer in the scaffold. The gibbsite particles were disk-like with a polydisperse distribution of diameters ranging from 0.2 μm to 1.25 μm. The average and standard deviation of the diameters, obtained by SEM imaging of 50 randomly-chosen particles, were found to be 0.56 μm and 0.24 μm, respectively.

Silica nanoparticles (NexSil 6 with 6 nm size and NexSil 125A with 85 nm size, Nyacol, Ashland, MA) and amidine latex nanoparticles (Invitrogen, Life Technologies, Grand Island, NY) with average size of 20 nm were used to create the nano-scale active layer in the membranes.

Preparation of the porous membranes. The porous membranes were fabricated using a procedure described previously[23–25,32]. In brief, suspensions containing specific amounts of silica nanoparticles and kaolinite particles were transferred into a stainless steel mold (40 mm diameter, 200 μm to 500 μm adjustable thickness) and allowed to gel upon the addition of 0.5 M NaCl. Immediately after gelation, the sample, along with the mold, was placed in a Freeze Dryer (SP Industries VirTis, Gardiner, NY) for freezing and drying. Afterward, the green sample was sintered at 1250°C for 1 h with a thin zirconia plate placed on top of it to maintain its disk-like shape throughout the sintering. The prepared porous membranes possessed a thickness of ~450 μm and a diameter of ~35 mm.

Infiltration of the micro-particles. Droplets of a 0.3 vol% micro-particle suspension with 0.066 g/mL PVP (average molecule weight M_n = 40000, Sigma Aldrich, St. Louis, MO) addition were placed onto the prepared porous scaffold. Since the pores of the scaffold are order of microns in size and also interconnected, the suspension rapidly penetrates the porous membrane. The amount of suspension was controlled to barely immerse the membrane. Samples were then left to dry in air. When the membranes became completely dry, heat treatment of 1000°C for 2 h was applied in order to fuse the infiltrated micro-particles in place. It should be note that membranes infiltrated with latex microspheres were not prepared with PVP addition and not subjected to heat treatment and the characterization measurements described below were instead performed immediately after the drying step.

Deposition of the nanoparticles. To create an active layer with nano-scale pores, membranes with micro-scale domains, created as described above, were first O_2-plasma cleaned (200 mTorr, 5 min, 100 W) and exposed immediately to TMCS (99+%, Sigma-Aldrich, St. Louis, MO) vapor overnight. This step rendered all of the surfaces in the membrane hydrophobic. Sulfuric acid solution (98 wt% H_2SO_4, Spectrum Chemicals & Laboratory Products, Gardena, CA) and hydrogen peroxide solution (30 wt% H_2O_2, Sigma-Aldrich, St. Louis, MO) were diluted to 1/10 concentration by volume and mixed at ratio of 3 : 1 (H_2SO_4 solution to H_2O_2 solution) to make a piranha solution. The hydrophobic membranes were then immersed in the piranha solution for 3 s, followed by spin-coating a 1 vol% nanoparticle aqueous suspension with 0.066 g/mL PVP addition at 2000 rpm for 1 min. The piranha solution removed the hydrophobic groups on the outer surface of the membrane and provided a nanometer-thickness hydrophilic region. By maintaining the bulk of the membrane hydrophobic with the exception of a thin hydrophilic layer near the face, the extent of penetration of the aqueous nanoparticle solution into the membrane could be controlled (i.e., the nanoparticle suspension did not infiltrate the hydrophobic regions of the membrane). The coated membranes were then dried in air and thermally treated at 850°C for 4 h.

Characterization. The microstructures of the membranes with and without infiltrating particles were examined by a field emission scanning electron microscope (SEM, LEO1550, Carl Zeiss MicroImaging Inc., Thornwood, NY). A ~3 nm Au-Pt layer was sputter coated on the samples before observation. Both the top faces (i.e., the face of the disk-shaped membrane containing the active layer) and the cross-sections (i.e., top to bottom) of the membranes were studied. The pore size distribution was measured using nitrogen adsorption−desorption measurements (Autosorb-1 C, Quantachrome Instruments, Boynton Beach, FL). To test the permeability and filtration ability, membranes were firstly mounted on a filtration setup with aluminum foil and silica rubber, leaving an exposed area with known dimensions. Deionized water or 0.01 vol% suspensions containing 100 nm (Polyscience Inc., Warrington, PA), 22 nm (Ludox TMA, Sigma Aldrich, St. Louis, MO), or 12 nm (Ludox AM, Sigma Aldrich, St. Louis, MO) silica particles were passed through the membranes under a fixed differential pressure (between 0.3 bar and 1 bar). The permeability was calculated by recording the amount of fluid passing through the membrane in a known time.

The rejection rate of the 12 nm and 22 nm nanoparticles was calculated by measuring the concentration in both the feed and filtrate suspensions. Particle concentration in each solution was determined by measuring the intensity of light scattered by the solution using a Zetasizer Nano ZS instrument (Malvern Instruments Ltd., Malvern, U.K.). Calibration tests showed that for each suspension, the scattered intensity varied approximately linearly with concentration and could thus be used as a convenient method for measuring concentration. (Supporting Information, Figure S4). The rejection rates of different nanoparticles were calculated by comparing the particle concentrations before and after the filtration.

For the 100 nm nanoparticles, it was found that the concentration in the filtrate was too low to provide a measurable scattered intensity. Thus for the tests with these nanoparticles, the rejection rate was determined by measuring the area density of deposited nanoparticles produced when a diluted and controlled volume drop of the suspension was placed on a glass slide and imaged by SEM. The suspensions were first diluted by a factor of 50 and then 50 μL of each suspension was placed on a 1 cm^2 glass slide. After drying, the glass slides were imaged with SEM. (The dilution helped generate a more uniform distribution of nanoparticles on the slide.) The rejection ratio was determined by comparing the resulting area density of the feed and filtrate suspensions. (It should be noted that this technique was also performed with the 12 nm and 22 nm nanoparticles and the resulting rejection rates were similar to those obtained using light scattering.)

The backwashing tests were performed by passing deionized water through the membrane under a controlled differential pressure in a direction opposite to that used during filtration. The membrane surface after backwashing was then imaged with SEM.

1. Ulbricht, M. Advanced functional polymer membranes. *Polymer* **47**, 2217–2262 (2006).
2. Carta, M. *et al*. An efficient polymer molecular sieve for membrane gas separations. *Science* **339**, 303–307 (2013).
3. Gin, D. L. & Noble, R. D. Designing the next generation of chemical separation membranes. *Science* **332**, 674–676 (2011).
4. Krieg, E., Weissman, H., Shirman, E., Shimoni, E. & Rybtchinski, B. A recyclable supramolecular membrane for size-selective separation of nanoparticles. *Nature Nanotechnol.* **6**, 141–146 (2011).
5. Kros, A., Nolte, R. J. M. & Sommerdijk, N. A. J. M. Conducting polymers with confined dimensions: Track-etch membranes for amperometric biosensor applications. *Adv. Mater.* **14**, 1779–1782 (2002).
6. Lai, Z. P. *et al*. Microstructural optimization of a zeolite membrane for organic vapor separation. *Science* **300**, 456–460 (2003).
7. de Vos, R. M. & Verweij, H. High-selectivity, high-flux silica membranes for gas separation. *Science* **279**, 1710–1711 (1998).
8. Ismail, A. F. & David, L. I. B. A review on the latest development of carbon membranes for gas separation. *J. Membrane Sci.* **193**, 1–18 (2001).
9. Chung, T. S., Jiang, L. Y., Li, Y. & Kulprathipanja, S. Mixed matrix membranes (MMMs) comprising organic polymers with dispersed inorganic fillers for gas separation. *Prog. Polym. Sci.* **32**, 483–507 (2007).
10. Baumann, S., Meulenberg, W. A. & Buchkremer, H. P. Manufacturing strategies for asymmetric ceramic membranes for efficient separation of oxgyen from air. *J. Eur. Ceram. Soc.* **33**, 1251–1261 (2013).
11. Nishizawa, M., Menon, V. P. & Martin, C. R. Metal nanotubule membranes with electrochemically switchable ion-transport selectivity. *Science* **268**, 700–702 (1995).
12. Wimley, W. C. & White, S. H. Experimentally determined hydrophobicity scale for proteins at membrane interfaces. *Nature Struct. Mol. Biol.* **3**, 842–848 (1996).
13. Lee, S. B. *et al*. Antibody-based bio-nanotube membranes for enantiomeric drug separation. *Science* **296**, 2198–2200 (2002).
14. Nunes, S. P. *et al*. Switchable pH-responsive polymeric membranes prepared via block copolymer micelle assembly. *ACS Nano* **5**, 3516–3522 (2011).
15. Park, M. H., Subramani, C., Rana, S. & Rotello, V. M. Chemoselective nanoporous membranes via chemically directed assembly of nanoparticles and dendrimers. *Adv. Mater.* **24**, 5862–5866 (2012).
16. Ke, X. B., Zhu, H. Y., Gao, X. P., Liu, J. W. & Zheng, Z. F. High-performance ceramic membranes with a separation layer of metal oxide nanofibers. *Adv. Mater.* **19**, 785–790 (2007).
17. Shannon, M. A. *et al*. Science and technology for water purification in the coming decades. *Nature* **452**, 301–310 (2008).
18. Jackson, E. A. & Hillmyer, M. A. Nanoporous membranes derived from block copolymers: From drug delivery to water filtration. *ACS Nano* **4**, 3548–3553 (2010).
19. Ding, X. L., Cao, Y. M., Zhao, H. Y. & Wang, L. N. Interfacical morphology between the two layers of the dual-layer asymmetric hollow fiber membranes fabricated by co-extrusion and dry-jet wet-spinning phase-inversion techniques. *J. Membrane Sci.* **444**, 482–492 (2013).
20. Widjojo, N., Zhang, S. D., Chung, T. S. & Liu, Y. Enhanced gas separation performance of dual-layer hollow fiber membranes via substructure resistance reduction using mixed matrix materials. *J. Membrane Sci.* **306**, 147–158 (2007).
21. Widjojo, N., Chung, T. S. & Krantz, W. B. A morphological and structural study of Ultem/P84 copolyimide dual-layer hollow fiber membranes with delamination-free morphology. *J. Membrane. Sci.* **294**, 132–146 (2007).
22. Caro, J., Noack, M., Kolsch, P. & Schafer, R. Zeolite membranes – state of their development and perspective. *Micropor. Mesopor. Mater.* **38**, 3–24 (2000).
23. Li, W., Lu, K. & Walz, J. Y. effects of added kaolinite on sintering of freeze-cast kaolinite-silica nanocomposite. I. Microstructure and phase transformation. *J. Am. Ceram. Soc.* **95**, 883–891 (2012).
24. Li, W., Lu, K. & Walz, J. Y. Effects of added kaolinite on the strngth and porosity of freeze-cast kaolinite-silica nanocomposites. *J. Mater. Sci.* **47**, 6882–6890 (2012).
25. Li, W., Lu, K. & Walz, J. Y. Formation, structure and properties of freeze-cast kaolinite-silica nanocomposites. *J. Am. Ceram. Soc.* **94**, 1256–1264 (2011).
26. Deville, S. In situ X-ray radiography and tomography obersevations of the solidification of aqueous alumina particle suspensions. Part I: Initial instants. *J. Am. Ceram. Soc.* **92**, 2489–2496 (2009).
27. Deville, S. In situ X-ray radiography and tomography obersevations of the solidification of aqueous alumina particle suspensions. Part II: Steady state. *J. Am. Ceram. Soc.* **92**, 2497–2503 (2009).
28. Routh, A. F. Drying of thin colloidal films. *Rep. Prog. Phys.* **76**, 1–30 (2013).
29. Kanai, T. & Sawada, T. New route to produce dry colloidal crystals without cracks. *Langmuir* **25**, 13315–13317 (2009).
30. Vohs, J. M. & Gorte, R. J. High-performance SOFC cathodes prepared by infiltration. *Adv. Mater.* **21**, 943–956 (2009).
31. Hendren, Z. D., Brant, J. & Wiesner, M. R. Surface modification of nanostructured ceramic membranes for direct contact membrane distillation. *J. Membrane Sci.* **331**, 1–10 (2009).
32. Li, W., Lu, K. & Walz, J. Y. Fabrication of porous nanocomposites with controllable specific surface area and strength via suspension infiltration. *Langmuir* **28**, 16423–16429 (2012).

Acknowledgments

Financial support for this work was provided by the College of Engineering at the University of Kentucky. The work was performed in the Department of Chemical Engineering at Virginia Tech. The authors would like to thank Yuan Zhou and Dr. Bo Chen for sharing their spin-coater, Dr. Abby Whittington for sharing her BET instrument, and Dr. Kathy Lu for sharing her freeze dryer. The assistance from Michael Vaught at Virginia Tech in preparing the stainless steel mold is greatly appreciated.

Author contributions

W.L. did all the experiments. J.Y.W. directed the research. W.L. and J.Y.W. wrote the manuscript.

Additional information

Supplementary information accompanies this paper at http://www.nature.com/scientificreports

Competing financial interests: The authors declare no competing financial interests.

How to cite this article: Li, W.L. & Walz, J.Y. Porous Nanocomposites with Integrated Internal Domains: Application to Separation Membranes. *Sci. Rep.* **4**, 4418; DOI:10.1038/srep04418 (2014).